Supporting information

Polymer Composites with Hierarchical Architecture and Dielectric Particles for Efficiency Daytime Subambient Radiative Cooling

Qian Yue[a,1], Li Zhang[a,1*],Cheng-Yu He[b***], Bao-Hua Liu[b], Wei-Ming Wang[b], Zhong-Wei Lu[b], Gang Liu[b], Xiang-Hu Gao[b**]

[a] *Department of Physics School of Science, Lanzhou University of Technology, Lanzhou, 730050, P. R. China.*

[b] *Laboratory of Clean Energy Chemistry and Materials, State Key Laboratory of Solid Lubrication, Lanzhou Institute of Chemical Physics, Chinese Academy of Sciences, Lanzhou 730000, China*

[*] Corresponding author:
E-mail address:
zhangli@lut.edu.cn (Li Zhang)
gaoxh@licp.cas.cn (Xiang-Hu Gao)
hechengyu@licp.cas.cn (Cheng-Yu He)

Section 1. Passive daytime radiative cooling (PDRC) performance calculation

Section 1.1 Solar radiative

Solar radiation has a particularly large effect on daytime radiative cooling. Radiative cooling is a process of unbalanced heat transfer. When the thermal radiation absorbed by an object is greater than the thermal radiation it emits, the temperature of the object itself will rise, and the influence of thermal conduction and convection may offset or exceed the cooler cooling effect. The solar radiation absorbed by the cooler can be defined as P_{sun} in Eq (1):[1]

$$P_{sun}(T) = A\int_0^{\infty} d\lambda\varepsilon(\lambda,\theta_{sun})I_{AM1.5}(\lambda)$$

Where A represents the true area of the cooler, θ_{sun} is the angle where the radiator faces the sun; $I_{AM1.5}(\lambda)$ denotes the AM1.5, which generally represents the solar spectrum obtained in the mid-latitude region, and the energy is 1000 W m^{-2}.

Section 1.2 Cooler thermal radiation

Thermal radiation is usually generated by the interaction between the electromagnetic radiation generated by the internal surface of the material and the thermal motion of atoms on the surface. The generation of thermal radiation is closely related to the energy generated by the forced vibrations and transitions of electrons inside the material. The thermal radiation of the cooler is the process of self-dissipation under the influence of the external environment, and its own energy and entropy increase after being irradiated by the sun. The thermal radiation power by the cooler can be defined as P_{rad} in Eq (2):

$$P_{rad} = A\int_0^{2\pi} d\Omega cos\theta \int_0^{\infty} d\lambda I_{BB}(T,\lambda)\varepsilon(\lambda,\theta)$$

Where $\int_0^{2\pi} d\Omega = \int_0^{\pi/2} d\theta sin\theta$ is the angular integral of the hemisphere,

$\frac{2hc^2}{\lambda^5} \frac{1}{\exp\left[\frac{hc}{\lambda k_B T}\right] - 1}$ is the spectral radiation intensity of the black body at temperature T, where h is Planck's constant and k_B is Boltzmann constant, c is the speed of light, and λ is the wavelength. $I_{BB}(T,\lambda)$ is the spectral radiation intensity of a black body at temperature T.

Section 1.3 Atmospheric thermal radiation

The Earth's surface is enveloped in an atmosphere rich in water vapor, and nitrogen. They can attenuate ultraviolet rays from the sun and various radiation rays from outer space, but this translucency also blocks the thermal radiation emitted by the earth in outer space. Due to the combined effect of the gas species in the atmosphere and its temperature, there is a higher penetration rate in the part of 8 to 13 μm. The temperature of objects on the surface of the earth is about 30 °C, and the most intense waveband is located in the infrared (8-13 μm). This is the key to radiative cooling, which is derived from the thermal radiation principles, the atmospheric thermal radiation power by the cooler can be defined as P_{atm} in Eq (3):

$$P_{atm}(T) = A\int_0^{2\pi} d\Omega cos\theta \int_0^{\infty} d\lambda I_{BB}(T_{atm},\lambda)\varepsilon(\lambda,\theta)\varepsilon_{atm}(\lambda,\theta)$$

According to Kirchhoff's radiation law, the absorption rate of a radiative cooler can be replaced by its emissivity $\varepsilon(\lambda,\theta)$; the directional emissivity of the atmosphere is determined by the following formula: $\varepsilon_{atm}(\lambda,\theta) = 1 - t(\lambda)^{1/cos\theta}$, where $t(\lambda)$ represents the transmittance of the atmosphere in the vertical direction. The light intensity is $I_{AM1.5}(\lambda)$(1000 W m^{-2}).

Section 1.4 Non-radiative heat loss

There are three types of heat conduction, thermal radiation, thermal convection, and thermal conduction. When the cooler is in contact with the external environment, it is inevitable with external objects and the surrounding air to conduct heat transfer and to exchange heat by convection. When the temperature of the cooler is higher than the

external environment, the heat exchange process with the outside world increases the cooling power of the cooler, and the non-radiative heat loss of the cooler is negative, but for sub-ambient cooling, this exchange of thermal processes can negatively affect the minimum cooling temperature of the cooler. the non-radiative heat loss power by the cooler can be defined as P_{loss} in Eq (4):

$$P_{cond+conv}(T) = Ah_c(T_{amb} - T)$$

Where h_c is the non-radiative heat transfer coefficient describing the conduction and convection heat exchange process. T is the temperature of the cooler, T_{amb} is the ambient temperature.

Section 1.5 Thermal balance of daytime radiative cooling

According to the energy balance theory, when the cooler is facing the sky under the sun, it not only emits its own heat to the outside and provides cooling capacity, it will also be affected by the heat radiated from the sun and the energy radiated from the atmosphere, and finally will be affected by non-radiative factors, i.e. convection and conduction heat transfer. The net cooling power provided by a cooler for cooling effect can be defined as in Eq (5):

$$P_{rad} = P_{sun} - P_{atm} - P_{cond+conv}$$

Where P_{rad}, P_{sun}, P_{atm}, and $P_{cond+conv}$ are described in detail in the above.

Section 1.5 Solar reflectivity of the cooler

A reported method was used, the spectrally averaged solar reflectance was defined as:

$$R_{solar} = \frac{\int_{0.3\mu m}^{2.5\mu m} d\lambda I_{solar}(\lambda)R(\lambda)}{\int_{0.3\mu m}^{2.5\mu m} d\lambda I_{solar}(\lambda)}$$

Where $I_{solar}(\lambda)$, $R(\lambda)$ is the ASTM G173 global solar intensity, the spectral reflectivity at wavelength λ, respectively.

Section 1.6 Thermal emissivity of the cooler

The thermal emissivity in the atmospheric window band (8-13 μm) was defined as:

$$\varepsilon_{8-13\mu m} = \frac{\int_{8\mu m}^{13\mu m} d\lambda I_{BB}(T,\lambda)\varepsilon(\lambda)}{\int_{8\mu m}^{13\mu m} d\lambda I_{BB}(T,\lambda)}$$

Where $I_{BB}(T,\lambda)$ and $\varepsilon(\lambda)$ represent the spectral intensity emitted by a blackbody at the ambient temperature $T = 300\ K$ and spectral emissivity of the emitters.

Section 2. Finite-Difference-Time-Domain Simulations

The effects of the wrinkle structure and Al_2O_3 microspheres on the spectral characteristics of the coating were studied by FDTD. The reflectivity of the HPC-film was obtained by simulating the 9×9×10 μm coating with a 3D model with periodic boundary conditions. Rough surface was used to construct the basic model of the HPC-film. The heights of wrinkle structure was adjusted by changing the parameters of "Sigma-Rms". The plane wave is used as the light source, and the wavelength of the injected light is 0.3-2.5 μm. In the FDTD simulation, the Al_2O_3 microspheres size was set to 6 μm and the mesh size was set to 500 nm. Reflectance and transmittance were monitored using a frequency domain field monitor.

Section 3. Indoor radiative cooling property measurements.

A xenon lamp (NBeT HFX-300) with a radiative spectral energy distribution close to that of sunlight is used to simulate solar irradiance, and the distance between the xenon lamp and the test sample is adjusted to form a spatially uniform radiation power distribution (1000 $W \cdot m^{-2}$) on the surface of the sample. Place the test sample on a polystyrene film plate to reduce the influence of heat conduction in the surrounding space, cover it with a polyethylene film to prevent the influence of air heat convection, and use a multi-channel thermometer connected with two k-type thermocouples to record the HPC-film and ambient temperature, respectively.

Section 4. Figure S1 to S20

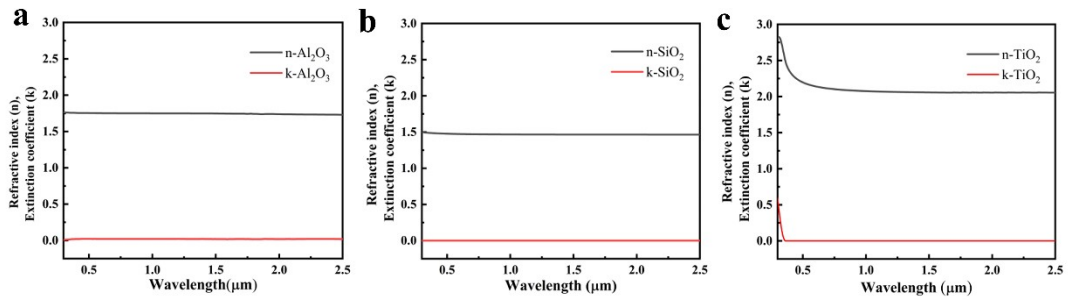

Fig. S1 Refractive index and extinction coefficient of (a) Al_2O_3, (b) SiO_2 and (c) TiO_2.

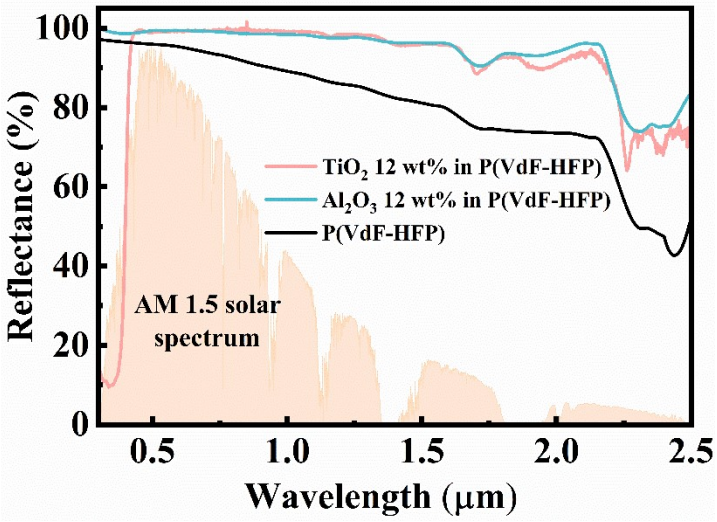

Fig. S2 Measured spectral reflectances of paints based on TiO_2, Al_2O_3, and porous P(VdF-HFP).

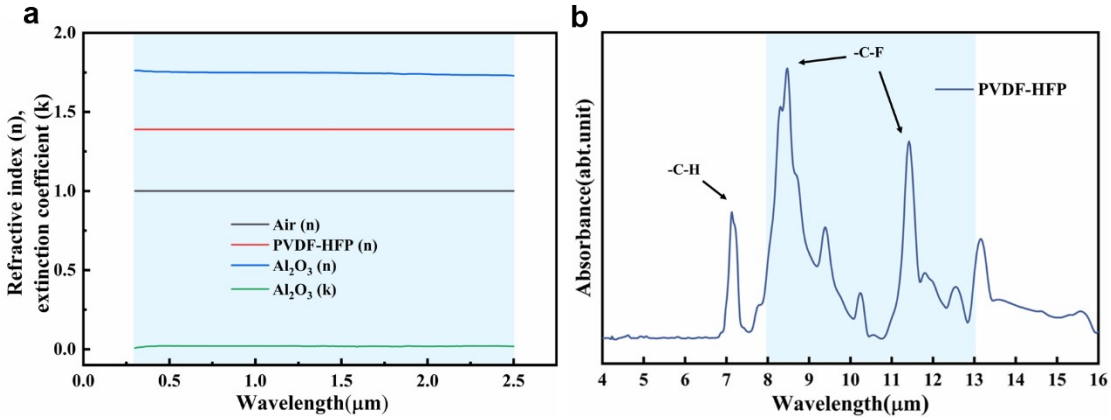

Fig. S3 (a) Refractive index contrast comparison of Al_2O_3 microspheres and P(VdF-HFP) materials with respect to air within the solar spectrum. (b) Absorbance spectrum of P(VdF-HFP) measured with ATR-FTIR spectroscopy.

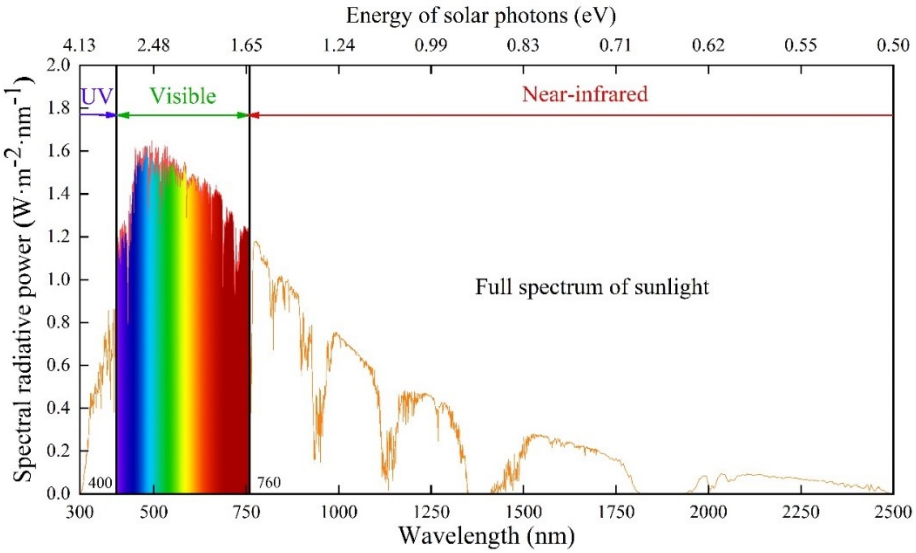

Fig. S4 Full spectrum of the solar and the energy distribution of solar photon.

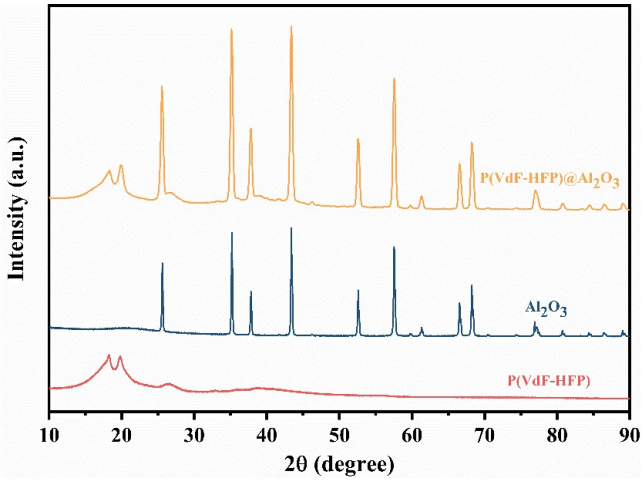

Fig. S5 XRD spectrum of the HPC-film

Supplementary Table 1 The surface chemical composition of the films determined using EDS analysis.

Sample	Element content (wt.%)			
	C	F	Al	O
	50.64	46.53	0.51	2.31

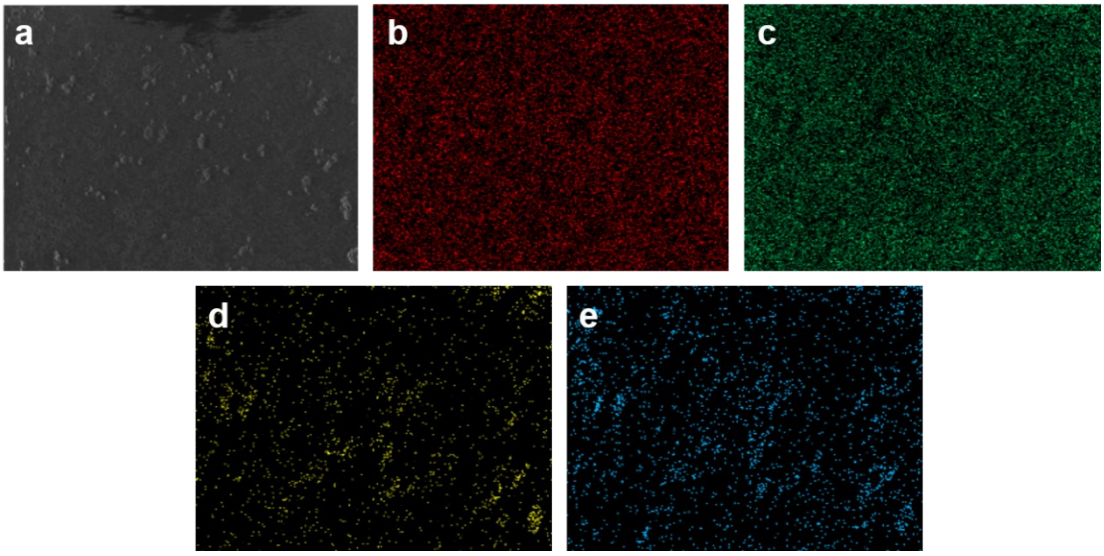

Fig. S6 EDS mapping images of the HPC-film. (a) SEM images**.** (b) Element C. (c) Element F. (d) Element Al. (e) Element O.

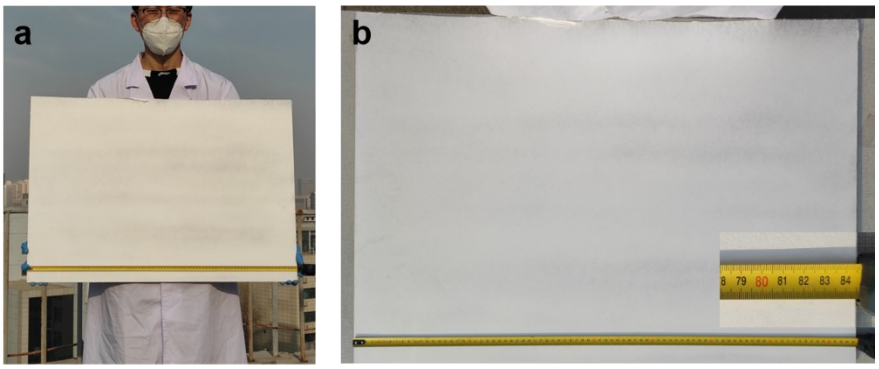

Fig. S7 Digital photo of HPC-film.

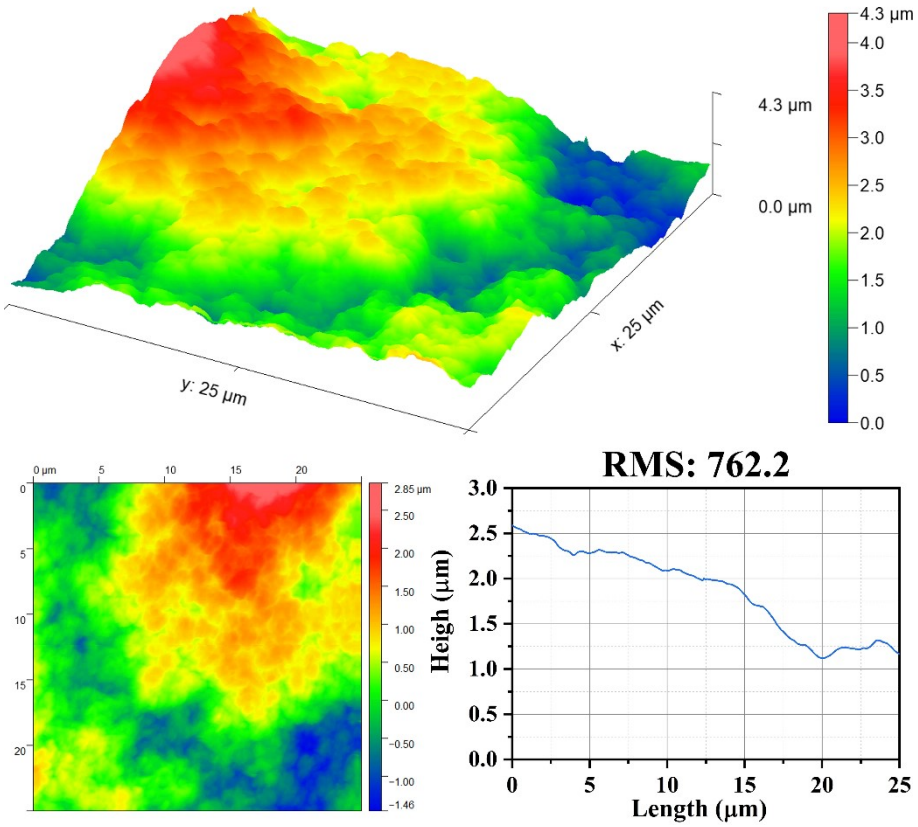

Fig. S8 3D topographies of the HPC film with large fluctuations

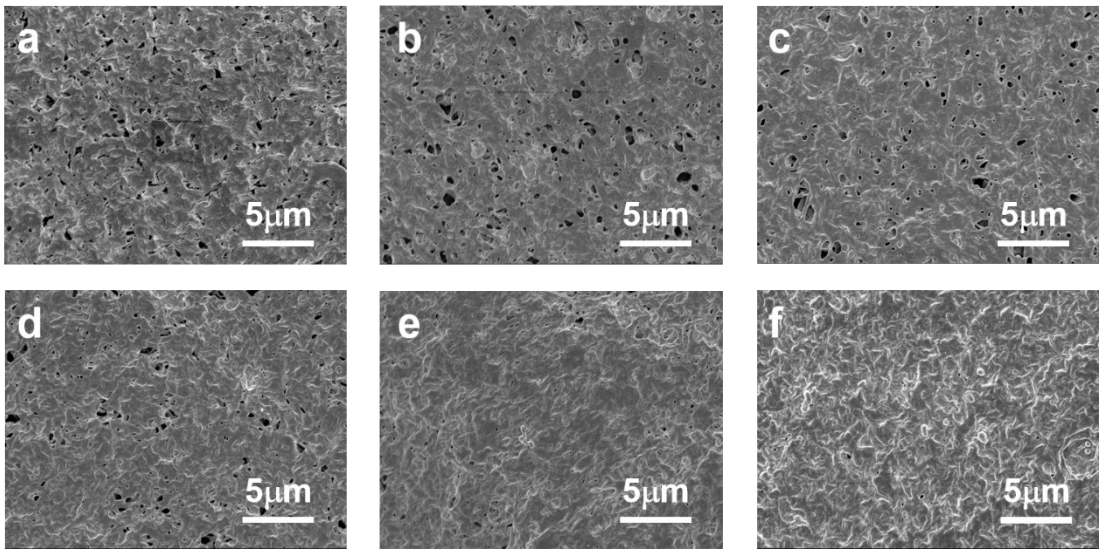

Fig. S9 The top-view SEM images of the HPC-films hybridized by Al_2O_3 microspheres with different mass fractions. (a) 0%; (b) 8%; (c) 10%; (d) 12%; (e) 14%; (f) 16%.

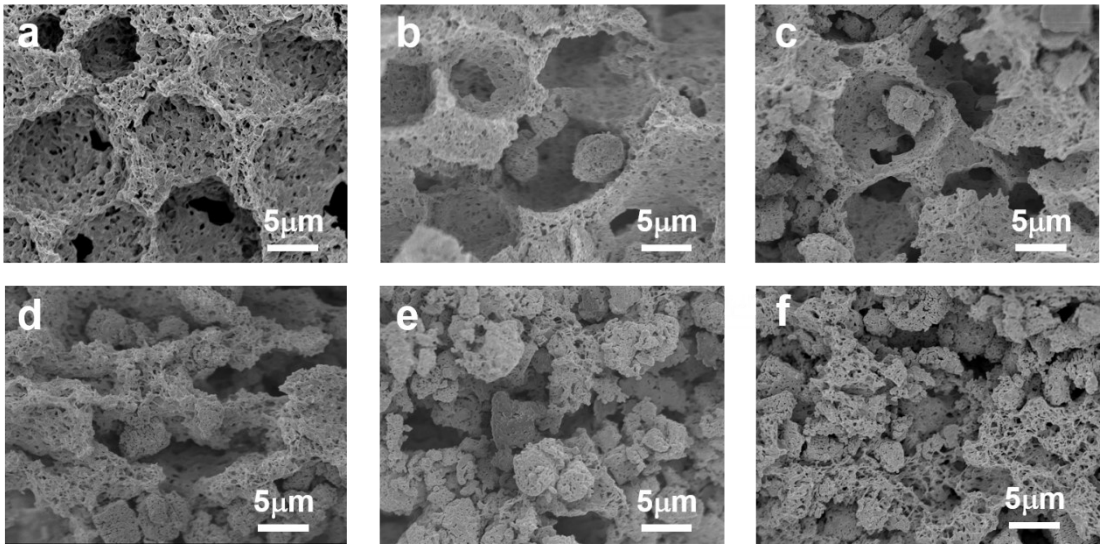

Fig. S10 The cross-view SEM images of the HPC-films hybridized by Al_2O_3 microspheres with different mass fractions. (a) 0%; (b) 8%; (c) 10%; (d) 12%; (e) 14%; (f) 16%.

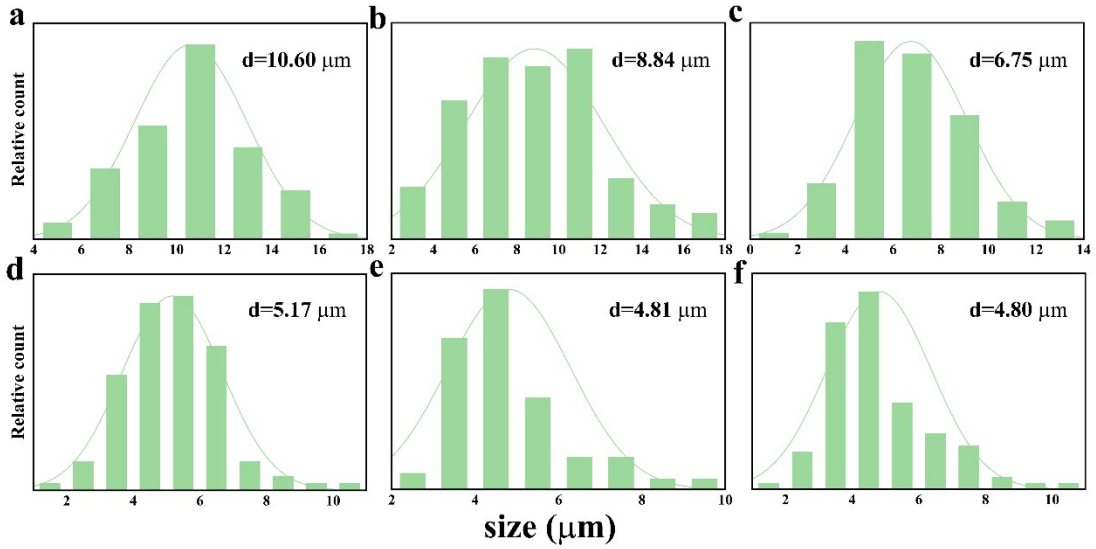

Fig. S11 Effects of different mass fractions of Al_2O_3 microspheres on the micropore size distribution of HPC-films. (a) 0%; (b) 8%; (c) 10%; (d) 12%; (e) 14%; (f) 16%.

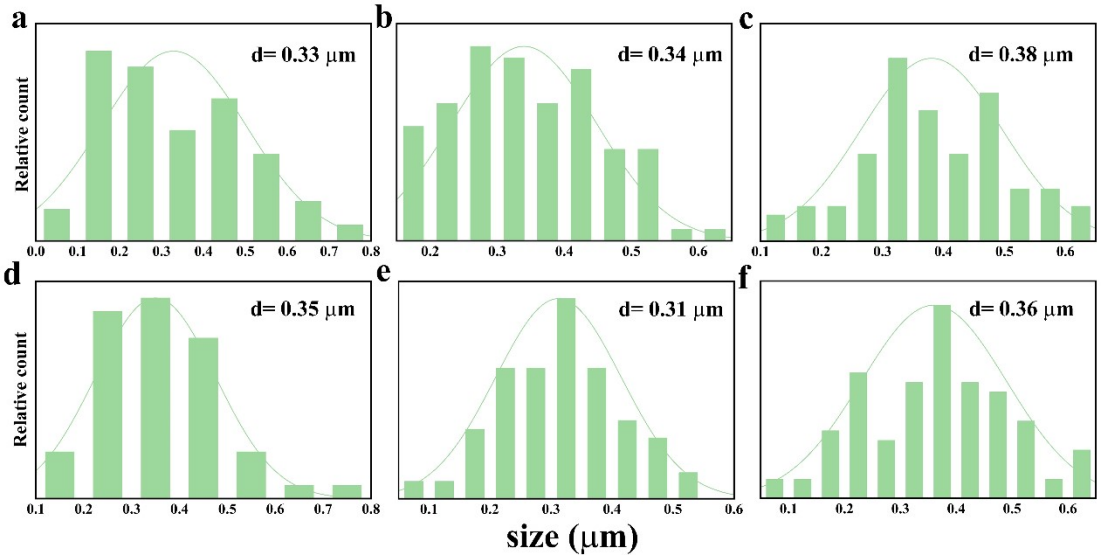

Fig. S12 Effects of different mass fractions of Al_2O_3 microspheres on the nanopore size distribution of HPC-films. (a) 0%; (b) 8%; (c) 10%; (d) 12%; (e) 14%; (f) 16%.

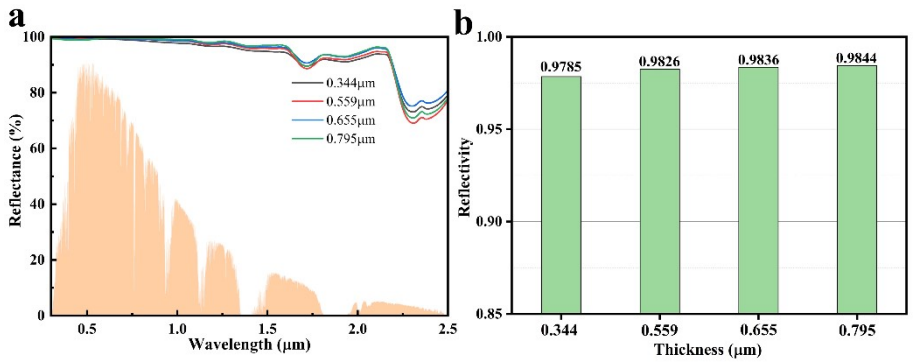

Fig. S13 Solar reflectance curves of HPC-film with different thicknesses. (a) Effect of the HPC-film thickness on the solar reflection (The thickness of the samples was 344 μm, 559 μm, 655 μm, and 795 μm, respectively). (b) Calculated solar reflectance (R_{solar}) by the standard solar irradiance of air mass 1.5 ($I_{AM}1.5$).

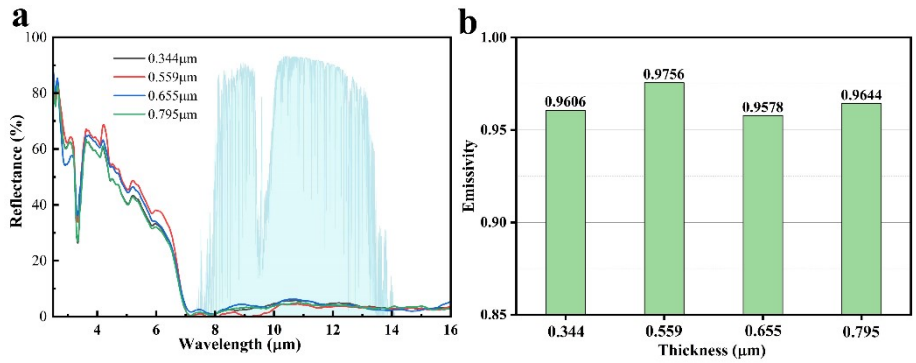

Fig. S14 Solar reflectance curves of HPC-film with different thicknesses. (a) Effect of

the HPC-film thickness on the solar emission (The thickness of the samples was 344 μm, 559 μm, 655 μm, and 795 μm, respectively). (b) Calculated solar emissivity rates at the atmospheric window (ε_{aw}) weighted by the spectral emittance of a blackbody (IBB).

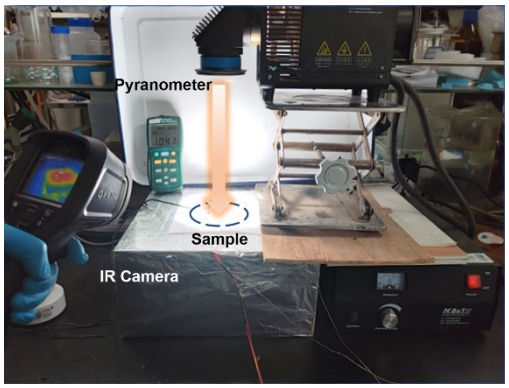

Fig. S15 Photo of the indoor experimental simulation device using a Xenon lamp (NBeT HFX-300) with a radiation spectral energy distribution close to that of sunlight is used to simulate solar radiation (The spectral range is 0.3-2.5 μm), and the distance between the xenon lamp and the test sample is adjusted to form a spatially uniform radiation power distribution (1000 W m^{-2}) on the surface of the sample.

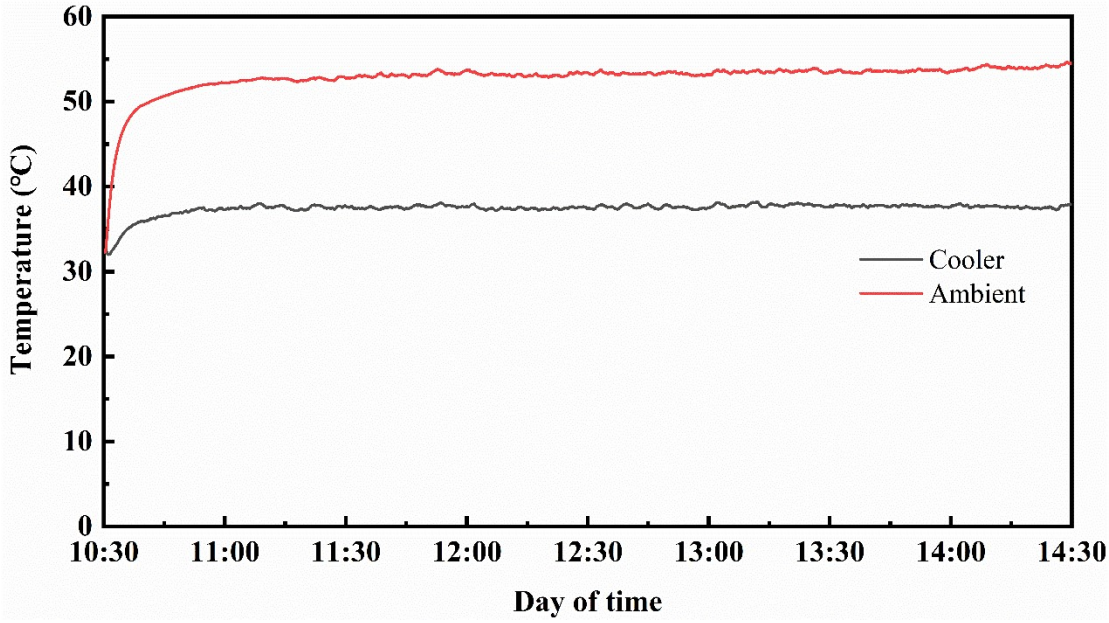

Fig. S16 Comparison of the temperature profiles of the HPC-films under I_{solar} =1000 W m^{-2}.

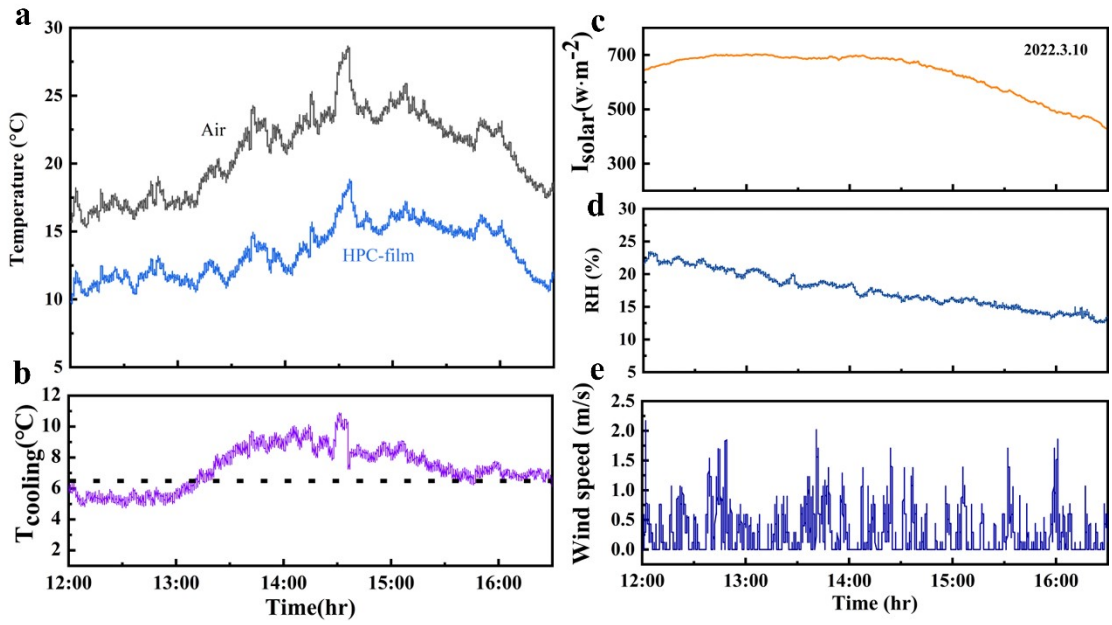

Fig. S17 Outdoor radiative cooling performance of HPC-film. (a) Temporal temperature data of the air and the HPC-film under direct sunlight and (b) the sub-ambient temperature drop (ΔT) of the HPC-film. (c) Solar intensity (I_{solar}) of the test location. (d) Relative humidity (RH) of the test location. (e) Wind speed of the test location.

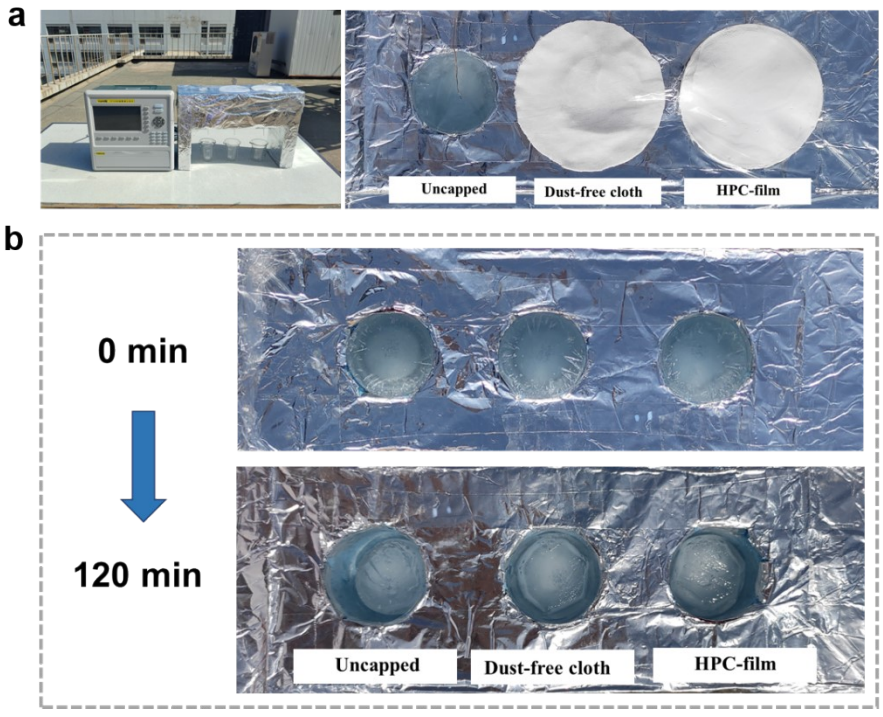

Fig. S18 (a) Experimental setup for verifying the cooling effects of the hierarchically designed HPC-film for ice. (c) The photographs show the evolution of the ice mass from the beginning to the end of the test.

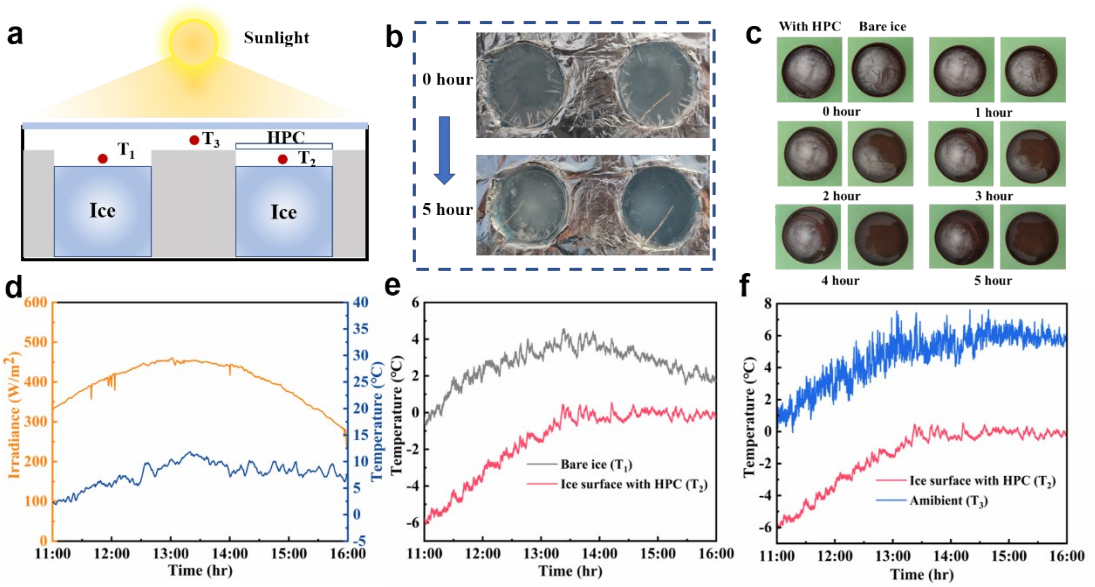

Fig. S19 Ice and snow protection of HPC film. (A) A schematic of the custom-made device for verifying the cooling effects of the HPC film for ice. (B)The photographs show the evolution of the ice mass from the beginning to the end of the test. (C) Photographs show the mass evolution of ice with (left) and without (right) the HPC film. (D) Variation of solar irradiance and outdoor temperature with time during the test. (E) Comparison of the temperature of ice between with and without the HPC film. (F) Subambient cooling enabled by the HPC film under intense illumination of sunlight of ~400 W m^{-2}.

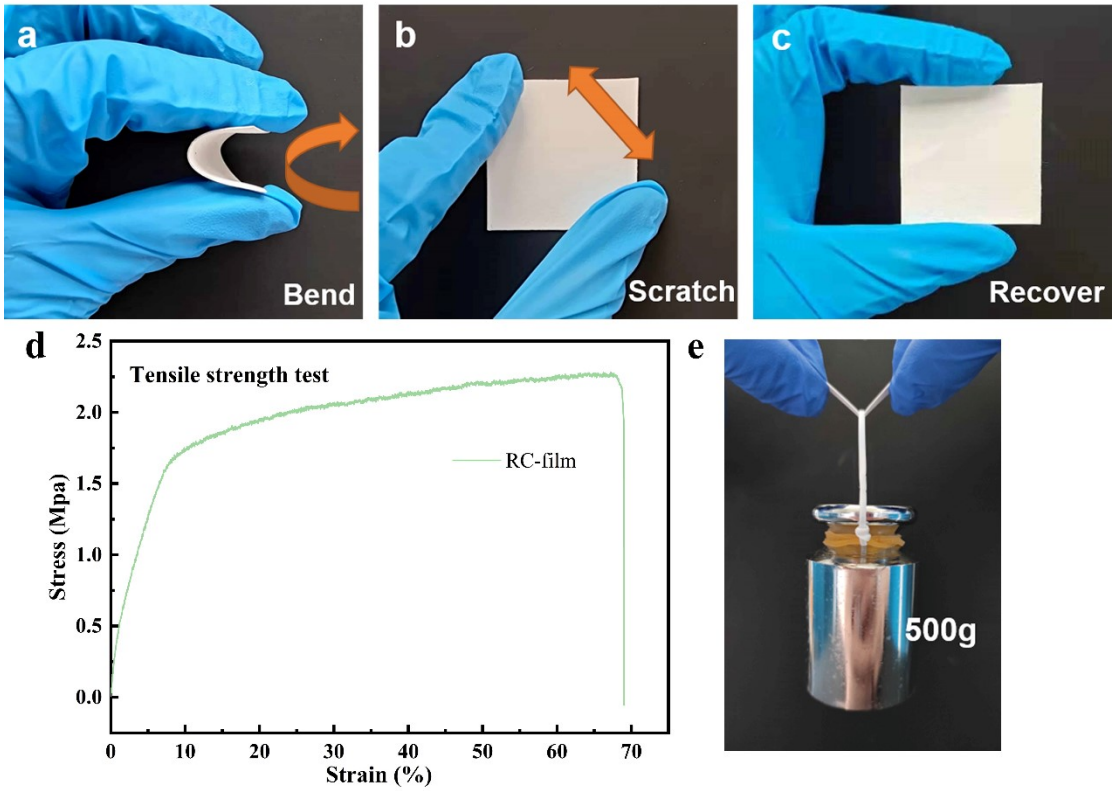

Fig. S20 Photos showing the flexibility and mechanical properties of the HPC-film.

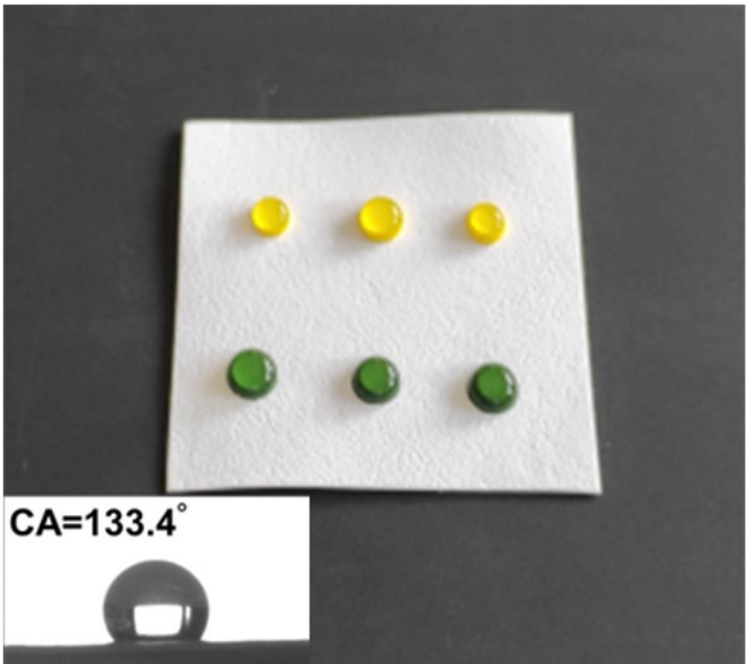

Fig. S21 The HPC-film with water droplets deposited on the surface with inset of the CA of 133.4°.

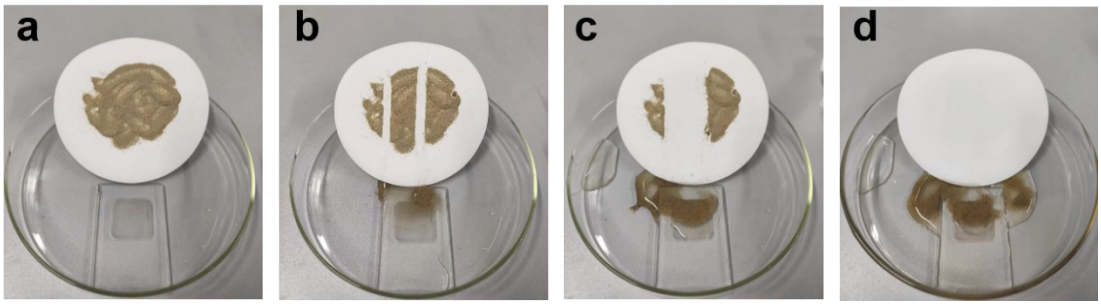

Fig. S22 Photographs of self-cleaning test of the HPC-film dust removed by water.

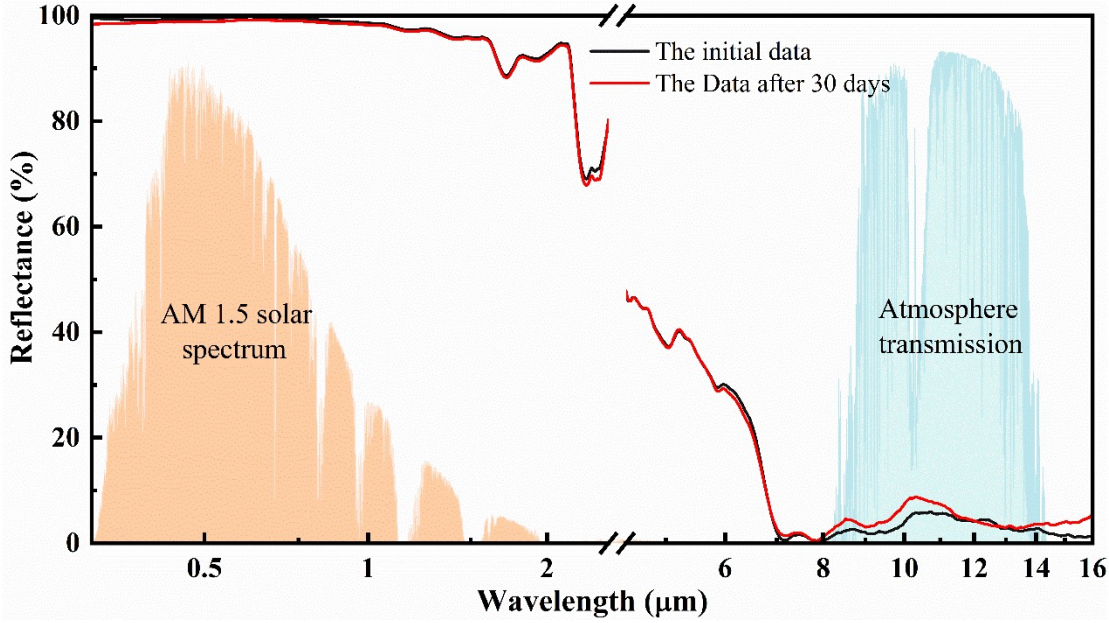

Fig. S23 The experimental reflectivity (1-emissivity) of the HPC-film before and after 30 days of exposure.

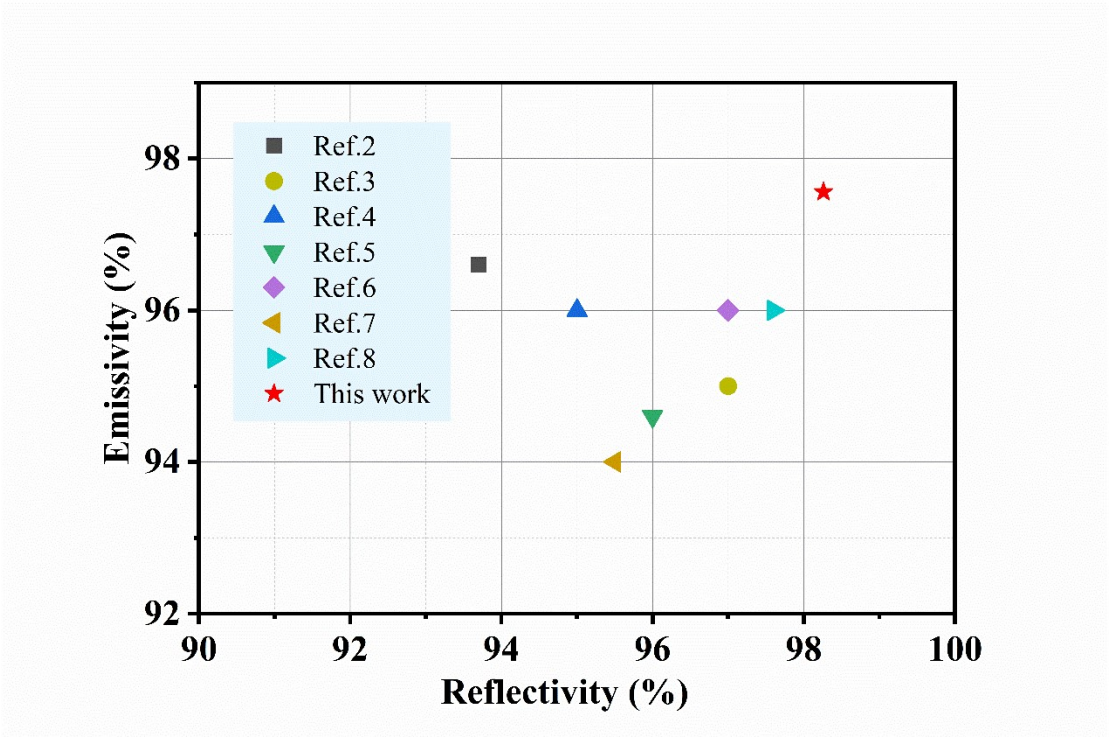

Fig. S24 Comparison of the spectrum performance among state-of-art radiative cooling materials with HPC-film. Our work demonstrated excellent spectral selectivity.

Section 5. References

[1] A. P. Raman, M. A. Anoma, L. Zhu, E. Rephaeli and S. Fan , Nature, 2014, 515, 540-544.

[2] H. Ma, L. Wang, S. Dou, H. Zhao, M. Huang, Z. Xu and C. Huang, ACS App. Mater. Interfaces, 2021, 13, 19282-19290.

[3] W. Jing, S. Zhang, W. Zhang, Z. Chen, C. Zhang, D. Wu and H. Zhu, ACS App. Mater. Interfaces, 2021, 13, 29558-29566.

[4] H. Zhang, K. C. Ly, X. Liu, Z. Chen, M. Yan, Z. Wu and T. Fan, Proc. Natl. Acad. Sci, 2020, 117, 14657-14666.

[5] B. Xiang, R. Zhang, Y. Luo, S. Zhang, L. Xu, H. Min and X. Meng, Nano Energy, 2021, 81, 105600.

[6] X. Chen, M. He, S. Feng, Z. Xu, H. Peng, S. Shi and Y. Zhou, Opt. Mater, 2021, 120, 111431.

[7] X. Li, J. Peoples, Z. Huang, Z. Zhao, J. Qiu and X. Ruan, Cell Rep. Phys. Sci, 2020, 1, 100221.

[8] X. Li, J. Peoples, P. Yao, X. Ruan, ACS App. Mater. Interfaces, 2021, 13, 21733-21739.